

# A Combined Limit on the Neutrino Mass from Neutrinoless Double- $\beta$ Decay and Constraints on Sterile Majorana Neutrinos

Pawel Guzowski,<sup>1</sup> Luke Barnes,<sup>1</sup> Justin Evans,<sup>1</sup> Georgia Karagiorgi,<sup>1</sup> Nathan McCabe,<sup>1</sup> and Stefan Söldner-Rembold<sup>1</sup>

<sup>1</sup>*The University of Manchester, Manchester M13 9PL, United Kingdom*

(Dated: September 18, 2018)

We present a framework to combine data from the latest neutrinoless double- $\beta$  decay experiments for multiple isotopes and derive a limit on the effective neutrino mass  $m_{\beta\beta}$  using the experimental energy distributions. The combined limits on  $m_{\beta\beta}$  range between 130–310 meV, where the spread is due to different model calculations of nuclear matrix elements (NMEs). The statistical consistency ( $p$  values) between this result and the signal observation claimed by the Heidelberg-Moscow experiment is derived. The limits on  $m_{\beta\beta}$  are also evaluated in a  $(3 + 1)$  sterile neutrino model, assuming all neutrinos are Majorana particles.

PACS numbers: 23.40.-s, 14.60.Pq, 14.60.St

## I. INTRODUCTION

The observation of neutrinoless double- $\beta$  ( $0\nu\beta\beta$ ) decays would demonstrate the Majorana nature of neutrinos [1], representing direct evidence for physics beyond the standard model. Neutrinoless double- $\beta$  decay is a second-order electroweak process where a nucleus decays through the emission of two electrons,  $(A, Z) \rightarrow (A, Z + 2) + 2e^-$ , thereby violating lepton number. The half-life of the isotope decaying through  $0\nu\beta\beta$  decay is given by

$$[T_{1/2}^{0\nu}]^{-1} = G^{0\nu} |M^{0\nu}|^2 \frac{m_{\beta\beta}^2}{m_e^2}, \quad (1)$$

assuming the exchange of a light Majorana neutrino (mass mechanism). Here,  $m_e$  is the electron mass. The phase space factors  $G^{0\nu}$  and nuclear matrix elements  $M^{0\nu}$  vary with isotope. The decay rate is proportional to the square of the effective neutrino mass  $m_{\beta\beta}$ , which represents a coherent sum over the masses  $m_i$  of the neutrino mass eigenstates,

$$m_{\beta\beta} = \left| m_1 |U_{e1}|^2 + m_2 |U_{e2}|^2 e^{i\alpha} + m_3 |U_{e3}|^2 e^{i\beta} \right|, \quad (2)$$

weighted by the squares of the corresponding elements  $U_{ei}$  of the Pontecorvo Maki Nakagawa Sakata (PMNS) matrix and the Majorana phases  $\alpha$  and  $\beta$ .

The seesaw mechanism is the most common model for neutrino mass generation [2]. Here, heavy right-handed neutrinos mix with the left-handed neutrinos and generate light Majorana masses for the active neutrinos. In addition to the exchange of these light Majorana neutrinos, there are several other potential models [3] that could contribute to  $0\nu\beta\beta$  decays, e.g., left-right symmetric models,  $R$ -parity violating supersymmetry, or models with extra dimensions. Observing  $0\nu\beta\beta$  decays with different isotopes could help to disentangle these mechanisms [4].

The search for  $0\nu\beta\beta$  decays is pursued in a range of experiments that use different isotopes. Experiments where

detector material and  $0\nu\beta\beta$  isotope are identical are constrained in the choice of isotope by the detector technology. This approach is employed by collaborations such as GERDA [5], which uses a high-purity  $^{76}\text{Ge}$  detector, EXO-200 [6] and KamLAND-Zen [7], which contain enriched  $^{136}\text{Xe}$ , and CUORICINO [8] and CUORE-0 [9], bolometers made of  $\text{TeO}_2$  crystals containing  $^{130}\text{Te}$ . Alternatively, detector and isotope can be separated, which allows experiments such as NEMO-3 [11] to study a variety of isotopes, e.g.,  $^{100}\text{Mo}$  and  $^{82}\text{Se}$ .

It is therefore important to develop techniques to combine the data taken by different experiments with a range of isotopes. This allows us to make quantitative comparisons between experiments, to study the consistency of their results, and to obtain combined limits on  $m_{\beta\beta}$ . A previous comparison of different experimental results using the published limits on  $T_{1/2}^{0\nu}$  has been performed in Ref. [12]. In this analysis, we simultaneously fit the experimental energy distributions to obtain a combined limit.

Such a direct combination of the results for multiple isotopes requires a specific NME calculation to relate the half-lives of the various isotopes before deriving a limit on  $m_{\beta\beta}$ . We chose a set of commonly used NME models to perform the combinations, but the procedure is generally applicable to include any NME model. The combination of the experimental energy distributions is performed for each particular NME model. In principle, different models could give a better estimate of the NMEs for different isotopes, but this case is not considered here, since it would require determining systematic correlations between the different models. The final limits on  $m_{\beta\beta}$  are given as a range covering the full set of NME models, following the procedure normally employed by individual experiments. We take into account theoretical uncertainties on the calculations where they are available.

In this Article, we present a method based on the published energy distributions from all recent experiments and use it to derive a first combined limit on  $m_{\beta\beta}$  based on multiple isotopes. We first demonstrate that we can

reproduce the published half-life limits of each individual experiment, before performing the combination using different NME calculations. We study the consistency of the combined  $m_{\beta\beta}$  limit with the positive claim of the Heidelberg-Moscow experiment [13]. We also interpret the combined limit on  $m_{\beta\beta}$  as a constraint on a  $(3 + 1)$  model with three active and one sterile Majorana neutrinos.

## II. METHOD

Limits are calculated using the  $CL_s$  method [14–16], which applies a modified-frequentist approach using a Poisson log-likelihood ratio (LLR) test statistic. The value of  $CL_s$  is defined as the  $p$  value of the data under the hypothesis that we observe both signal and background,  $CL_{sb}$ , divided by the  $p$  value for the background-only hypothesis ( $CL_b$ ). Systematic uncertainties are marginalized through Gaussian constraints on the priors, with the best fits of these parameters determined by maximizing the likelihood with respect to the data in both the signal-plus-background and background-only hypotheses. A limit at the 90% Confidence Level (CL) is obtained from the signal strength that produces a value of  $CL_s = (100 - 90)\%$ . The expected limit corresponds to the median of an ensemble of pseudo-experiments generated from the background-only probability distributions, and the  $\pm 1$  standard deviation ranges are derived from the ensemble. When combining multiple experiments, the limit setting process uses a sum of the experiments' individual LLRs, assuming no correlations.

For a single experiment, the signal strength is inversely proportional to the half-life  $T_{1/2}^{0\nu}$ . When combining multiple experiments, the signal strength is calculated for a common  $m_{\beta\beta}$ , which is related to  $T_{1/2}^{0\nu}$  using Eq. 1 and for a specific NME calculation.

## III. EXPERIMENTAL INPUTS

The most stringent published limits on neutrinoless double- $\beta$  decay are currently provided by the CUORICINO, CUORE, EXO-200, KamLAND-Zen, GERDA, and NEMO-3 experiments. We use their most recent published energy distributions, together with the statistical and systematic uncertainties on signal and backgrounds, and the correlations of the systematic uncertainties as quoted by the experiments. The input distributions are shown in Fig. 1 with their statistical uncertainties. In total, we combine 250 data points. The experimental systematic uncertainties are assumed to be uncorrelated between experiments, because the data are taken using completely different experimental approaches.

CUORICINO was a bolometric detector comprising 62 TeO<sub>2</sub> crystals, which were operated between 2003 and 2008, for a total exposure of 19.75 kg·y [8]. Using this exposure and the average signal efficiency of 82%, we

obtain a total expected number of 18 signal decays for a half-life of  $2.8 \times 10^{24}$  years. The energy distribution for the signal published in Fig. 9 of Ref. [8] normalized to this decay rate is used as the input distribution for the limit setting. We use an uncertainty for the signal normalization of 1.5% and an energy scale uncertainty of 0.8 keV. A normalization uncertainty of 4.2% is applied for the constant background, and the <sup>60</sup>Co background, which is centred at an energy of 2505 keV, has a normalization uncertainty of 7.7%. These background uncertainties are the exposure-weighted statistical uncertainties taken from Table 4 of Ref. [8].

The CUORE experiment has also published results from a first phase, CUORE-0, which utilizes a single tower with 52 TeO<sub>2</sub> crystals. The results correspond to an exposure of 9.8 kg·y for the isotope <sup>130</sup>Te. We use the data published in Fig. 3 of Ref. [9] and the reported signal efficiency of  $(81.3 \pm 0.6)\%$ . The signal shape is taken from Ref. [10], parametrized by a Gaussian function with width of  $\approx 5$  keV. The statistical uncertainty on the background normalization is 3.45%, whereas the effect of other systematic uncertainties is negligible.

The EXO-200 detector contains a liquid xenon time projection chamber that has been in operation since 2011 [6]. A total of 200 kg of xenon is used, with <sup>136</sup>Xe enriched to 81%. We use the energy distribution of the single-site (SS) decays published by the EXO-200 Collaboration in Fig. 4(a) of Ref. [6] for an exposure of 100 kg·y, since the sensitivity of SS topologies to  $0\nu\beta\beta$  decays is significantly higher than for multi-site (MS) topologies. We apply a signal normalization uncertainty of 8.6% with an energy scale uncertainty of 0.2%. The background normalization uncertainty is 10.9%. We also apply an overall normalization uncertainty of 9.6%, correlated between signal and background distributions, which is derived from the ratio of SS to MS topologies.

The KamLAND-Zen detector is filled with 13 tons of liquid scintillator, which is loaded with enriched <sup>136</sup>Xe [7]. We use Fig. 1(a) of Ref. [7], published after a total exposure 89.5 kg·y with a background normalization uncertainty of 11.21% and a signal normalization uncertainty of 3.99%.

The GERDA Collaboration uses high-purity germanium calorimeters enriched in <sup>76</sup>Ge [5]. We use the dataset obtained between 2011 and 2013 [5], with an exposure of 21.6 kg·y. The energy distribution is taken from Fig. 1 of Ref. [5] after pulse shape discrimination. We apply a 9% uncertainty on the signal normalization and a 20% uncertainty on the constant background normalization.

The NEMO-3 Collaboration took data from 2003 to 2011 with a tracker-calorimeter detector measuring seven  $0\nu\beta\beta$  candidate isotopes [11]. Since the <sup>100</sup>Mo measurements are the most sensitive due to the larger isotope mass, we focus on this isotope. The input distribution is the data shown in Fig. 2 of Ref. [11], which corresponds to an exposure of 34.7 kg·y. The signal normalization uncertainty is 7%, and the normalization uncertainty are 0.7% for the two-neutrino background and 10% for the

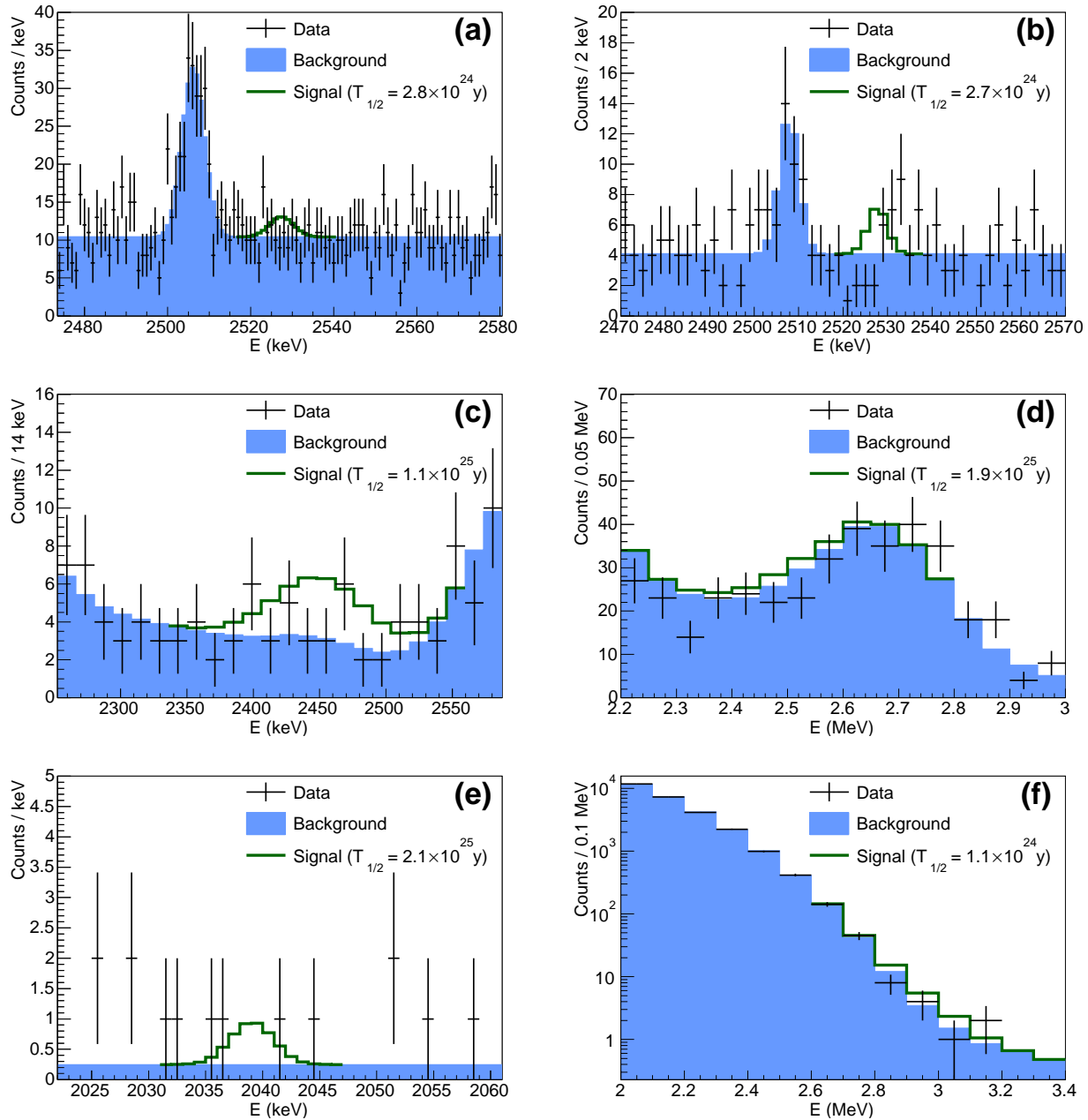


FIG. 1: Energy distributions for signal and background used as input for the combination with their statistical uncertainties: (a) CUORICINO, (b) CUORE-0, (c) EXO-200, (d) KamLAND-Zen, (e) GERDA, and (f) NEMO-3 data. The signal distributions are normalized to represent the 90% CL observed limits.

other backgrounds.

We expect small differences between our method and the published results, since we use a different limit setting procedure and only a single input distribution for each experiment. As a first step designed to validate our method, we determine the lower limits on the half-lives at the 90% CL and compare them to the values published by the collaborations (see Table I). The results for  $^{76}\text{Ge}$  and  $^{100}\text{Mo}$  are in very good agreement with the published values. The half-life limit for the EXO-200 data

are 15% – 20% higher with our limit setting method, whereas the result for KamLAND-Zen is about 10% lower. We observe the same effect for a previously published EXO-200 result [17], which has also been used by the KamLAND-Zen Collaboration to set a combined limit for  $^{136}\text{Xe}$  [7]. We combine the same two  $^{136}\text{Xe}$  data sets and obtain a limit of  $T_{1/2}^{0\nu} = 34 \times 10^{24}$  y, in perfect agreement with the published KamLAND-Zen combination.

We also obtain perfect agreement for the CUORICINO result using  $^{130}\text{Te}$ , while the limit on  $T_{1/2}^{0\nu}$  obtained by the

Experiment	Limit on $T_{1/2}^{0\nu}$ ( $10^{24}$ y)				
	Publ.	Obs.	Exp.	$\pm 1\sigma$ range	$1-CL_b$
<b><math>^{130}\text{Te}</math>:</b>					
CUORICINO	2.8 [8]	2.8	2.9	2.0 – 4.2	0.474
CUORE-0	2.7 [9]	3.0	3.0	2.1 – 4.3	0.520
Combined	4.0 [9]	4.4	4.3	2.9 – 6.2	0.513
<b><math>^{136}\text{Xe}</math>:</b>					
EXO-200	11 [6]	13	21	14 – 30	0.131
KamLAND-Zen	19 [7]	17	11	7 – 15	0.918
Combined	—	21	24	16 – 34	0.360
<b><math>^{76}\text{Ge}</math>:</b>					
GERDA	21 [5]	20	21	14 – 29	0.450
<b><math>^{100}\text{Mo}</math>:</b>					
NEMO-3	1.1 [11]	1.1	0.9	0.6 – 1.4	0.634

TABLE I: The published limits on  $T_{1/2}^{0\nu}$  for each experiment are compared to the calculated observed and expected limits. The  $\pm 1\sigma$  range around the expected limit and the  $1-CL_b$  value of the data are also shown.

CUORE-0 Collaboration is 10% lower than the limit we derive. Since CUORICINO and CUORE-0 are two phases of the same experiment, we only use the combined CUORE limit to perform our remaining analysis.

The observed limits are also compared to the median expected limits and the corresponding  $\pm 1\sigma$  range around the median expected limits. All observed limits lie within the  $\pm 1\sigma$  band, except for the KamLAND-Zen result, where the observed limit of  $T_{1/2}^{0\nu} = 17 \times 10^{24}$  y is about  $1.5\sigma$  better than the expected limit, corresponding to  $1-CL_b$  of 0.918. This is caused by the deficit of data compared to the background expectation in the signal region.

#### IV. NUCLEAR MATRIX ELEMENTS

We derive limits on the effective neutrino mass for different NME calculations, which are summarized in Table II. The five different models used in the combination are the Generating Coordinate Method (GCM) [18], the Interacting Boson Model (IBM-2) [19], the Interacting Shell Model (NSM) [20], and three models using the Quasiparticle Random-Phase Approximation: (i) the QRPA model using four different sub-calculations based on the Argonne V18 (A) or charge-dependent Bonn (B) nucleon-nucleon potentials with an older (*old*) or newer (*new*) version of the parametrization of the particle-particle interactions [21], (ii) the proton-neutron QRPA model (pnQRPA) [22], and (iii) a QRPA model that uses its renormalized version for evaluating uncertainties, labelled (R)QRPA [23].

The model calculations predict values for the NMEs which can differ by up to a factor of  $\approx 2$  for a particular isotope. The NSM model predicts the smallest NMEs for all isotopes, apart from  $^{100}\text{Mo}$  which is not evaluated in this calculation, whereas the models differ in their predictions of the isotopes with the largest NMEs.

The (R)QRPA and the IBM-2 calculations also provide

uncertainties on the NMEs. The IBM-2 model uncertainties on the NMEs are 16%, which we have assumed to be fully correlated across isotopes. The (R)QRPA model includes a correlation matrix between isotopes, which we take into account in the limit setting. The uncertainties are evaluated in Ref. [23] by using (i) two values of the weak axial-vector coupling parameter,  $g_A = 1$  and 1.25, (ii) two different approaches to short-range correlations, (iii) two many-body models, QPRA and RQPRA, and (iv) three different sets of single-particle states. The uncertainties also include the experimental uncertainties on the particle-particle coupling constant  $g_{pp}$  extracted from  $2\nu\beta\beta$  data. The resulting 24 combinations are used to extract correlation coefficients from the error ellipses which cover the full range of possible outcomes. For our experimental combination, we reinterpret these model uncertainties as Gaussian uncertainties by reducing them by a factor of 0.68. We quote the reduced uncertainties in Table II.

The phase space factors  $G^{0\nu}$  are taken from a recent calculation [24]. We set the weak axial-vector coupling parameter to  $g_A = 1.27$ . The uncertainties on the phase space factors originate from the uncertainties on the  $Q$  values and the nuclear radius. The uncertainty on the nuclear radius dominates and leads to an uncertainty on the phase space factor  $G^{0\nu}$  of  $\approx 7\%$ .

#### V. RESULTS

Only in the case of  $^{136}\text{Xe}$ , two independent experiments, KamLAND-Zen and EXO-200, measured the same isotope. Their data can be combined directly without using NMEs to derive a limit on  $T_{1/2}^{0\nu}$ . The combination yields a limit of  $T_{1/2}^{0\nu} > 2.1 \times 10^{25}$  y, which is dominated by the EXO-200 measurement due to the higher exposure compared to KamLAND-Zen. This observed value is less stringent than the previously published combined value of  $T_{1/2}^{0\nu} > 3.4 \times 10^{25}$  y [7] based on a smaller EXO-200 data set [17], which displays a downward fluctuation of the data relative to the background expectation. The combined sensitivity, given by the median expected limit, has improved from  $T_{1/2}^{0\nu} = 1.6 \times 10^{25}$  y to  $T_{1/2}^{0\nu} = 2.4 \times 10^{25}$  y due to the increased exposure.

To combine results for multiple isotopes, we include the effects of NMEs. We show an example in Fig. 2 for the GCM calculation. The results for  $m_{\beta\beta}$  are shown for each individual experiment, ordered by their sensitivities using this model. The combined observed limit is  $m_{\beta\beta} < 130$  meV for an expected limit of  $m_{\beta\beta} < 130$  meV, which improves upon the best individual limit obtained by KamLAND-Zen of  $m_{\beta\beta} < 150$  meV and the best individual expected limit by EXO-200 of  $m_{\beta\beta} < 140$  meV. All limits are given at the 90% CL. Since the mass limit depends on the fourth root of the exposure, these improvements corresponds to an increase in exposure by a factor of 1.4–1.6.

Isotope	Phase Space Factor $G^{0\nu}$ ( $10^{-14}y^{-1}$ ) [24]	Nuclear Matrix Element Models													
		GCM IBM-2 NSM			QRPA [21]				pnQRPA [22]		(R)QRPA [23]				
		[18]	[19]	[20]	A-old	A-new	B-old	B-new		NME	Rel. Unc.	Correlation Matrix			
$^{76}\text{Ge}$	0.615	4.60	4.68	2.30	5.812	5.157	6.228	5.571	5.26	4.315	0.191	1			
$^{100}\text{Mo}$	4.142	5.08	4.22	—	5.696	5.402	6.148	5.850	3.90	3.184	0.254	0.973	1		
$^{130}\text{Te}$	3.699	5.13	3.70	2.12	4.306	3.888	4.810	4.373	4.00	3.148	0.247	0.899	0.862	1	
$^{136}\text{Xe}$	3.793	4.20	3.05	1.76	2.437	2.177	2.735	2.460	2.91	1.795	0.293	0.805	0.747	0.916	1

TABLE II: Phase space factors for  $g_A = 1.27$  for the four isotopes, values of the nuclear matrix elements for the GCM, IBM-2, NSM, QRPA, pnQRPA, and for the (R)QRPA NME calculation, together with the relative uncertainties on the (R)QRPA NMEs and their correlation matrix. The relative uncertainties quoted for the IBM-2 calculation are 0.16 for each isotope.

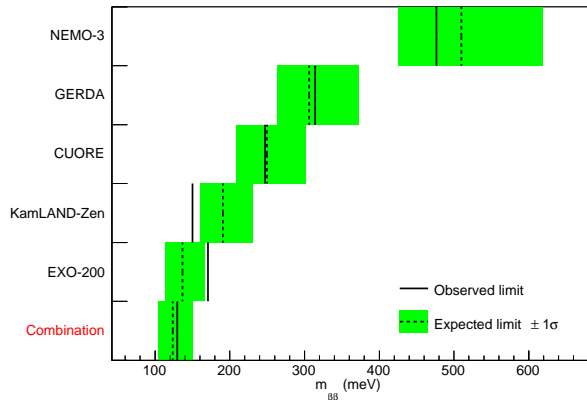


FIG. 2: Individual experiment effective mass limits, and the combined limit, using the GCM model.

Using the GCM model, the CUORE and GERDA data have sensitivities of  $m_{\beta\beta} = 250$  meV and 310 meV, respectively, while the two experiments using  $^{136}\text{Xe}$  have the best sensitivities in the range  $m_{\beta\beta} = 140$ –190 meV. Figure 3 shows the observed and expected limits for each

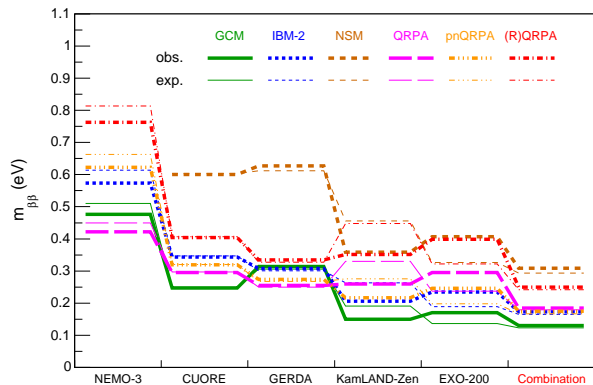


FIG. 3: Observed and expected limit on  $m_{\beta\beta}$  for the different experiments and NME models without NME model uncertainties.

NME model and experiment separately. For this comparison, NME uncertainties are not taken into account, since

only some of the calculations provide them. The ordering of the experimental sensitivities changes with the NME model used to derive the  $m_{\beta\beta}$  limit, further emphasising the need for using a range of isotopes to search for  $0\nu\beta\beta$  decays.

The coefficients of the correlation matrix provided by the (R)QRPA calculations for the four isotopes considered here range from 0.747 to 0.973 (see Table II). To study the effect of these correlations, we derive the limits on  $m_{\beta\beta}$  assuming no NME uncertainties, the full correlation matrix, and a single correlation coefficient for all isotope combinations ranging from  $-0.3$  to 1. The

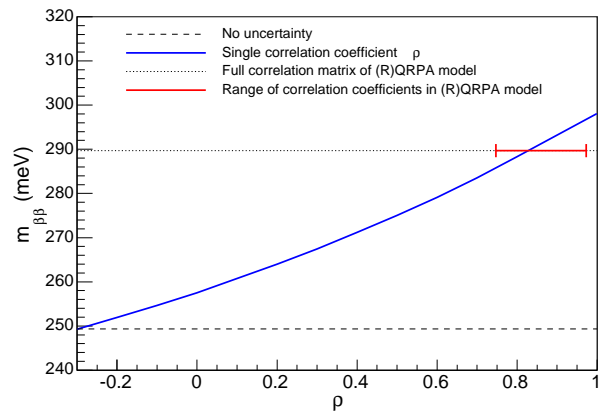


FIG. 4: Limit on  $m_{\beta\beta}$  as a function of a single correlation coefficient  $\rho$  in the (R)QRPA model. The lines at  $m_{\beta\beta} = 250$  meV and 290 meV represent the limits without uncertainties and with the full correlation matrix of the (R)QRPA model, respectively. The red line shows the range of correlation coefficients.

results are shown in Fig. 4. Using no NME uncertainties yields a limit of  $m_{\beta\beta} < 250$  meV, which increases to  $m_{\beta\beta} < 290$  meV once the model uncertainties and the full correlation matrix are taken into account, and to  $m_{\beta\beta} < 300$  meV assuming 100% correlation between the NME uncertainties for the different isotopes. The variation in limits of  $\approx 40$ –50 meV is comparable to the range observed for the different model assumptions with the QRPA calculation, which are expected to represent similar model uncertainties.

In Table III, we show the combined limits on  $m_{\beta\beta}$  for

NME	$m_{\beta\beta}^{\text{obs}}$	$m_{\beta\beta}^{\text{exp}}$	Improvement		$p$ value (HM)
	(meV)	(meV)	Limit	Sensitivity	
GCM	130	120	14% (K)	10% (E)	0.001
IBM-2:					
no unc.	170	170	16% (K)	12% (E)	0.010
with unc.	190	180	16% (K)	13% (E)	0.021
NSM	310	290	14% (K)	10% (E)	0.003
QRPA:					
A-new	200	200	23% (G)	25% (E)	0.095
A-old	180	180	26% (G)	25% (E)	0.100
B-new	180	180	28% (K)	24% (E)	0.073
B-old	170	160	28% (K)	23% (E)	0.077
pnQRPA	170	170	19% (K)	16% (E)	0.029
(R)QRPA:					
no unc.	250	240	25% (G)	25% (E)	0.109
with unc.	290	290	23% (G)	21% (G)	0.311

TABLE III: For each NME calculation, the combined observed and expected limits on  $m_{\beta\beta}$ , the improvement in the limit and the sensitivity relative to the best individual experiments for that NME model. The best experiments are GERDA (G), EXO-200 (E), or KamLAND-Zen (K). The  $p$  value of the limit with respect to the Heidelberg-Moscow (HM) positive claim [13] are also shown. All  $m_{\beta\beta}$  limits are given to two significant digits.

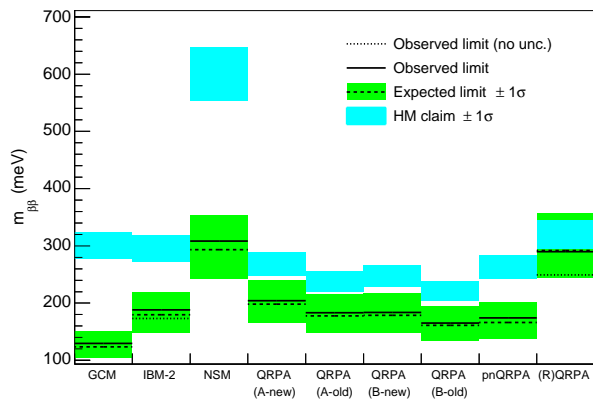


FIG. 5: Mass limits (observed and expected) for each NME calculation. For the IBM-2 and (R)QRPA models, the limits are given both with and without the uncertainty on the NME calculation. The effective mass for the positive Heidelberg-Moscow (HM) claim [13] is also shown.

each NME model. We provide the observed and expected limits for each combination and the improvements in observed limit and sensitivity over the result obtained by the best individual experiment. As shown in Fig. 3, the most sensitive experiments change for the different models.

The combined results are compared to the result obtained by the Heidelberg-Moscow (HM) experiment in Fig. 5, where the error bands represent the uncertainties of the HM half-life measurement of  $T_{1/2}^{0\nu} = (2.23^{+0.44}_{-0.31}) \times 10^{25}$  y for  $^{76}\text{Ge}$  [13]. The  $p$  values, testing the consistency

between the result obtained by the HM experiment using  $^{76}\text{Ge}$  and the combined upper limits, are also given in Table III. They are calculated taking into account the experimental uncertainties.

The  $p$  values differ significantly between different NME models, and any conclusion on the level of consistency between the combination of the latest experimental results and the result obtained with the the  $T_{1/2}^{0\nu}$  reported by the HM group depends strongly on the chosen NME model. The  $p$  values range from 0.001 (about 3 standard deviations) for the GCM model to 0.311 for the (R)QRPA models. The  $p$  value for the GERDA result and this HM measurement is 0.63, independent of NME model since the experiments both use the isotope  $^{76}\text{Ge}$ .

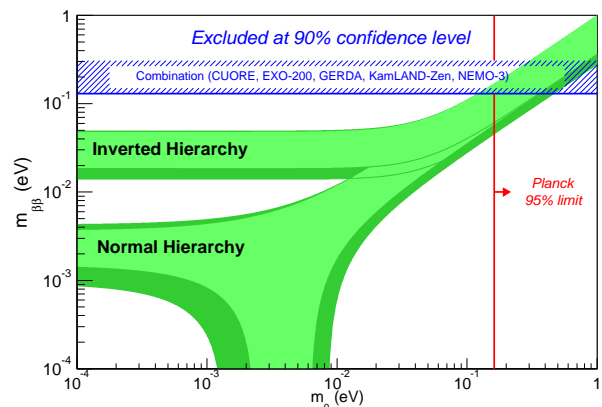


FIG. 6: Combined limits on the effective mass  $m_{\beta\beta}$  as a function of the lightest neutrino mass  $m_0$ . The width of the horizontal band represents the range of limits obtained with the different NME models. The neutrino oscillation parameters are taken from Ref. [25], using the best fit values. The inner band for the NH and IH fits shows the full range associated with the unknown Majorana phases and the outer band the additional effect of the 3-standard deviation experimental uncertainties on the oscillation parameters. The limit on  $m_0$  derived from the Planck data is also shown.

The best published limit on  $m_{\beta\beta}$  by KamLAND-Zen [7] is obtained by combining their data with the earlier EXO-200 result [17]. Using a similar set of NMEs, the mass range they obtain is  $m_{\beta\beta} = 120\text{--}250$  meV, whereas our observed combined limit in the range  $m_{\beta\beta} = 130\text{--}310$  meV is slightly higher because we use the latest EXO-200 data set.

In Fig. 6, we overlay the range of observed combined limits on the allowed effective mass  $m_{\beta\beta}$  as a function of the lightest neutrino mass  $m_0$ , with the bands representing current measurement uncertainties of the neutrino oscillation parameters assuming either the normal hierarchy (NH) with  $m_1 < m_2 < m_3$  or the inverted hierarchy (IH) with  $m_3 < m_1 < m_2$  for the ordering of the neutrino mass eigenstates in the standard three-neutrino framework. We also show a limit on  $m_0$ , which is derived from the limit on the sum of the neutrino masses obtained by the Planck Collaboration [26]. They set a limit

of  $\sum_i m_i < 492$  meV at the 95% CL based on the temperature and the polarization of the Cosmic Microwave Background.

We also interpret the combined limit on  $m_{\beta\beta}$  as a constraint on a single sterile Majorana neutrino that mixes with the three active Majorana states. In this model, the expression for the effective neutrino mass  $m_{\beta\beta}$  defined in Eq. 2 is modified to take into account the mixing with the fourth neutrino state:

$$m_{\beta\beta} = \left| m_1 |U_{e1}|^2 + m_2 |U_{e2}|^2 e^{i\alpha} + m_3 |U_{e3}|^2 e^{i\beta} + m_4 |U_{e4}|^2 e^{i\gamma} \right|. \quad (3)$$

It includes an additional mass term  $m_4$ , a Majorana phase  $\gamma$ , and the element  $U_{e4}$  of the now extended,  $4 \times 4$  mixing matrix, which is related to the sterile neutrino mixing angle  $\theta_{14}$  through  $|U_{e4}|^2 = \sin^2 \theta_{14}$  in the parametrization used here. In this model, the unitarity constraint applies only for the  $4 \times 4$  mixing matrix. However, the central values of the elements  $U_{ei}$  ( $i = 1, 2, 3$ ) do not change significantly when the  $3 \times 3$  unitarity constraint is removed from the global fit [27]. The unitarity constraint on the  $4 \times 4$  mixing matrix will restrict  $|U_{e4}|^2 = \sin^2 \theta_{14}$  to be  $\lesssim 0.1$ .

Our ability to probe a certain range of  $m_4 |U_{e4}|^2$  depends on  $m_0$  and the Majorana phases (see, e.g., [28, 29]). We take the approach of translating the limits on  $m_{\beta\beta}$  into corresponding limits on the combination  $m_4 |U_{e4}|^2$  under two extreme situations for a given  $m_0$ :

- The NME model (NSM) that predicts the highest (least stringent) limit on  $m_{\beta\beta}$ , together with the phases  $\alpha = \beta = 0$ , and  $\gamma = \pi$  that provide the smallest contribution to  $m_{\beta\beta}$ .
- The NME model (GCM) that predicts the lowest (most stringent) limit on  $m_{\beta\beta}$ , together with the phases  $\alpha = \beta = \gamma = 0$  that provide the largest contribution to  $m_{\beta\beta}$ .

This first parameter set allows for large contributions from  $m_4 |U_{e4}|^2$  and thus provides the least constraining limit on  $m_4 |U_{e4}|^2$ , whereas the second set allows for only small contributions from  $m_4 |U_{e4}|^2$  and thus yields the most constraining limit on  $m_4 |U_{e4}|^2$ .

In Figs. 7 and 8, we translate the measured combined limit on  $m_{\beta\beta}$  for the two situations above into a limit in the  $(m_4, |U_{e4}|^2)$  plane for a set of different assumptions on  $m_0$ . To be consistent with cosmological bounds, we vary  $m_0$  between 0 and 150 meV. For any of the  $m_0$  values considered, all other NME model and Majorana phase combinations will produce limit curves that lie in between these extremes. The values of  $\Delta m_{ij}^2$  and  $U_{ei}$  ( $i, j = 1, 2, 3$ ) are taken from a recent global fit [25]. Including the three-standard deviation uncertainties on these fit values has negligible effect on the results.

The central value of  $\sin^2 2\theta_{14} = 0.09$  and  $\Delta m_{41}^2 = 1.78$  eV<sup>2</sup> from a global fit [30] of the oscillation parameters in a (3+1) sterile neutrino model including reactor,

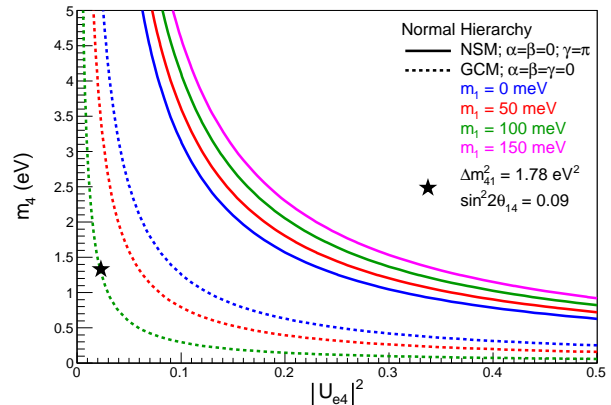


FIG. 7: Limits on  $m_{\beta\beta}$  for different NME models translated into a constraint on the sterile neutrino in the  $(m_4, |U_{e4}|^2)$  plane in a (3+1) model. Different values of the Majorana phases  $\alpha, \beta, \gamma$  and of the lightest active neutrino mass  $m_1$  in the NH are shown. The complete region is excluded for  $m_1 = 150$  meV with the GCM model and vanishing Majorana phases.

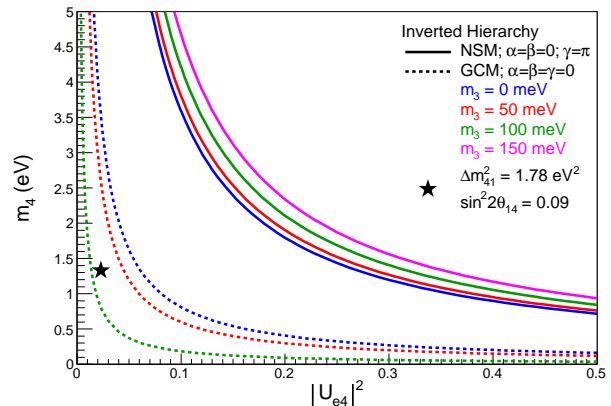


FIG. 8: Limits on  $m_{\beta\beta}$  for different NME models translated into a constraint on the sterile neutrino in the  $(m_4, |U_{e4}|^2)$  plane in a (3+1) sterile neutrino model. Different values of the Majorana phases  $\alpha, \beta, \gamma$  and of the lightest active neutrino mass  $m_3$  in the IH are shown. The complete region is excluded for  $m_3 = 150$  meV with the GCM model and vanishing Majorana phases.

gallium, solar neutrino, and LSND/KARMEN  $\nu_e$  disappearance data, all of which are directly sensitive to  $m_4$  and  $|U_{e4}|$ , is also shown in Figs. 7 and 8. The limit from the  $0\nu\beta\beta$  combined fit is currently close to the (3+1) global best fit value only in the more constraining scenarios calculated using the GCM model and with  $m_0 > 100$  meV and favorable Majorana phases. Our results are consistent with previous analyses (see, e.g., [29, 31]) that investigate  $m_{\beta\beta}$  regions allowed by global fits to oscillation experiments under a (3+1) hypothesis. Assuming the sterile neutrino is a Majorana particle, neutrinoless

double- $\beta$  decay can therefore independently constrain the existence of a sterile neutrino under those extreme assumptions. For a more detailed discussion on constraints to (3+1) sterile neutrino models from neutrinoless double  $\beta$  decay and projected implications for next-generation experiments, see Ref. [32].

## VI. SUMMARY

We have performed the first combination of the latest data sets from experiments searching for neutrinoless double- $\beta$  decay using multiple isotopes. Using the  $CL_s$  method, we set a limit on the effective neutrino mass  $m_{\beta\beta}$  in the range 130 – 310 meV, depending on NME model. Combining the data from multiple isotopes and experiments significantly increases the sensitivity over using the single-best experiment only, corresponding to an

increase by a factor of  $\approx 1.5 - 2.4$  in exposure. We compare these limits with the claimed observation of the Heidelberg-Moscow experiment and obtain  $p$  values that differ significantly depending on the NME calculations chosen, ranging from 0.001 for the GCM model to 0.31 for the (R)QRPA model. Using the uncertainties and the full correlation matrix provided by the (R)QRPA model changes the limit on  $m_{\beta\beta}$  by 40 – 50 meV compared to using no NME uncertainties. We also translate the combined limit on  $m_{\beta\beta}$  into a constraint on a light sterile Majorana neutrino in a (3 + 1) model. This translated limit is NME and  $m_0$  and Majorana phase dependent.

## Acknowledgements

We want to thank Fedor Šimkovic and Sean Freeman for useful discussions about the nuclear matrix elements.

- 
- [1] W. H. Furry, Phys. Rev. **56**, 1184 (1939).  
[2] For a recent review, see S.M. Bilenky and C. Giunti, Mod. Phys. Lett. A **27**, 1230015 (2012).  
[3] F. F. Deppisch, M. Hirsch, and H. Päs, J. Phys. G **39**, 124007 (2012).  
[4] R. Arnold *et al.* (SuperNEMO Collaboration), Eur. Phys. J. C **70**, 927 (2010).  
[5] M. Agostini *et al.* (GERDA Collaboration), Phys. Rev. Lett. **111**, 122503 (2013).  
[6] J. B. Albert *et al.* (EXO-200 Collaboration), Nature **510**, 229 (2014).  
[7] A. Gando *et al.* (KamLAND-Zen Collaboration), Phys. Rev. Lett. **110**, 062502 (2013).  
[8] E. Andreotti *et al.*, Astropart. Phys. **34**, 822 (2011).  
[9] K. Alfonso *et al.* (CUORE Collaboration), arXiv:1504.02454 [nucl-ex], submitted to Phys. Rev. Lett.  
[10] C. Tomei (CUORE Collaboration), INFN Seminar, 22 April 2015, pg. 56.  
[11] R. Arnold *et al.* (NEMO-3 Collaboration), Phys. Rev. D **89**, 111101(R) (2014).  
[12] A. Faessler, G. L. Fogli, E. Lisi, V. Rodin, A. M. Rotunno, and F. Šimkovic, Phys. Rev. D **87**, 053002 (2013).  
[13] H. Klapdor-Kleingrothaus and I. Krivosheina, Mod. Phys. Lett. A **21**, 1547 (2006).  
[14] T. Junk, Nucl. Instrum. Meth., A **434**, 435 (1999).  
[15] A. L. Read, J. Phys., G **28**, 2693 (2002).  
[16] W. Fisher, FERMILAB-TM-2386-E (2007).  
[17] M. Auger *et al.* (EXO Collaboration), Phys. Rev. Lett. **109**, 032505 (2012).  
[18] T. R. Rodriguez and G. Martinez-Pinedo, Phys. Rev. Lett. **105**, 252503 (2010). We use the values of Table I.  
[19] J. Barea, J. Kotila, and F. Iachello, Phys. Rev. C **91**, 034304 (2015). We use the values of Table I.  
[20] J. Menendez, A. Poves, E. Caurier, and F. Nowacki, Nucl. Phys. A **818**, 139 (2009). We use the values of Table 8 for the Jastrow short-range correlations.  
[21] F. Šimkovic, V. Rodin, A. Faessler, and P. Vogel, Phys. Rev. C **87**, 045501 (2013). We use the values of Tables II and III.  
[22] J. Hyvärinen and J. Suhonen, Phys. Rev. C **91**, 024613 (2015). We use the values of Table III.  
[23] A. Faessler, G. L. Fogli, E. Lisi, V. Rodin, A. M. Rotunno, and F. Šimkovic, Phys. Rev. D **79**, 053001 (2009). We use the values of Table I.  
[24] J. Kotila and F. Iachello, Phys. Rev. C **85**, 034316 (2012). We use the values of Table III.  
[25] M. Gonzalez-Garcia, M. Maltoni, and Th. Schwetz, J. High Energy Phys. **11**, 52 (2014).  
[26] P.A.R. Ade *et al.* (Planck Collab.), arXiv:1502.01589 [astro-ph.CO], submitted to Astronomy & Astrophysics (2015).  
[27] S. Parke and M. Ross-Lonergan, private communications.  
[28] Y. F. Li and S. S. Liu, Phys. Lett. B **706**, 406 (2012).  
[29] I. Girardi, A. Meroni, and S. T. Petcov, J. High Energy Phys. **11**, 146 (2013).  
[30] J. Kopp, P.A.N. Machado, M. Maltoni, and Th. Schwetz, J. High Energy Phys. **05**, 050 (2013).  
[31] C. Giunti, M. Laveder, Y. F. Li, Q. Y. Liu, and H. W. Long, Phys. Rev. D **86**, 113014 (2012); C. Giunti, M. Laveder, Y. F. Li, and H. W. Long, Phys. Rev. D **87**, 013004 (2013); A. Abada, V. De Romeri, and A. M. Teixeira, J. High Energy Phys. **09**, 074 (2014).  
[32] C. Giunti, E. M. Zavanin, arXiv:1505.00978 [hep-ph].